Extrinsic Calibration of a Ground Penetrating Radar

Chieh Chou, Shu-Hao Yeh, Jingang Yi, and Dezhen Song

Abstract— **To develop a multi-modal in-traffic bridge deck scanning device, we need to calibrate extrinsic parameters of a ground penetrating radar (GPR). GPR output is in a non-Euclidean coordinate system because it only detects underground objects relative to road surface. When road surface is non-planar, its output cannot be trivially mapped to a 3D Cartesian system which is necessary for sensor fusion. We design an artificial planar bridge as the calibration device to ensure that the GPR output maintains Euclidean coordinate property during the calibration process. The bridge also allows us to adjust metal balls as calibration objects. We model the GPR imaging process and extract readings from hyperbolas generated from metal balls. We employ the maximum likelihood estimator to estimate the rigid body transformation and provide the closed form error analysis. We have conducted physical experiments to validate our calibration process. Results show that the calibrated model has an average error of 9.77 mm for testing samples. This is satisfying because the GPR signal wave length is 18.8 cm.**

I. INTRODUCTION

We are interested in developing automatic scanning devices for in-traffic bridge deck inspection, which requires us to combine a ground penetrating radar (GPR) with a camera to form a multi-sensor suite that is capable of simultaneously performing both subsurface and surface inspection. Fusing the data from different sensors is nontrivial. Unlike the camera, the intrinsic 3D coordinate system of a GPR is not necessarily Euclidean because its horizontal plane is assumed to be overlapped with the road plane. When the road surface is non-planar, its output cannot be directly aligned with Euclidean 3D structure constructed from the camera. An indoor pre-calibration that estimates GPR extrinsic parameters (i.e. rotation and translation difference in coordinate systems) to establish coordinate system transformation between sensors is necessary. The first step to achieve this is to perform an extrinsic calibration on the GPR.

Here we propose a method for the extrinsic calibration of a GPR (see Figure 1). We design an artificial planar bridge as the calibration device to ensure the GPR output coordinate is Euclidean. Using metal balls as calibration objects, we model the GPR imaging process and extract hyperbolas in the GPR image to recover metal ball coordinates in the GPR coordinate system. Combining with direct position measurements in the world coordinate system, we can estimate the rigid body transformation relationship between the GPR local
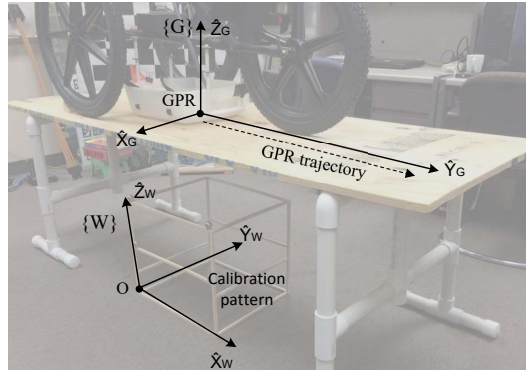
Fig. 1. Extrinsic calibration of a GPR. The GPR is mounted on a tri-wheel survey cart, and placed on the calibration platform. After moving along a straight line, the GPR registers a radargram. The radargram and the calibration patterns are inputs to the calibration problem. The coordinate system mapping between the world frame $\{W\}$ and the local frame $\{G\}$ is the output.

coordinate system and the world coordinate system. We also analyze the error propagation and present the closed form error distribution for our calibration results. We have tested our calibration method in physical experiments and results show that the calibrated model has an average error of 9.77 mm for testing samples. Considering the fact that the GPR signal wave length is 18.8 cm, the result is satisfying.

II. RELATED WORK

To improve the accuracy of a mechanism or a sensor, calibration is an indispensable technique which contains three main components: a model, measurements, and a parameter estimation process [1]. It begins with a closed-form geometry and/or physical model that characterizes a mechanism or a sensing phenomenon. A calibration process is to collect measurements to estimate the model parameters. The measurements are always noisy which is often described by statistical error models. The error models can be obtained either analytically or statistically. A Gaussian distribution is a common error model due to its robust asymptotic probability attributes in large populations [2]. The parameter estimation process finds the model parameters by minimizing an aggregated error metric function.

Mechanism calibration often solves the kinematic parameters and the inertial parameters for mechanisms with prismatic or revolute joints. Similar to the geometry model in the GPR extrinsic calibration problem, a kinematic model builds on a 6 degrees of freedom (DoF) rigid body transformation in a Cartesian coordinate system. In robotics and automation, mechanism calibration can be seen everywhere:

robot manipulator calibration [3], pan-tilt robotic cameras calibration [4], and hand-eye calibration [5].

Sensor calibration differs from mechanism calibration due to the unique combination of intrinsic calibration and extrinsic calibration. While the extrinsic model is the similar 6-DoF rigid body transformation, the intrinsic model describes the underlying physical principles for sensing [6]. Depending on different sensors, the corresponding calibration model varies and leads to different calibration problem: camera calibration [7], radio antenna calibration [8], LIDAR calibration [9], and calibration of different kinds of sensors [10]. Our problem belongs to extrinsic calibration which models GPR imaging characteristics and outputs 6-DoF rigid body transformation to describe its pose.

A GPR measures the time between echoes of electromagnetic signals to survey the objects and layers beneath the ground surface and has many important applications [11]–[13]. A GPR can be mounted on a robotic system for mine detection and removal [14], [15]. Also, GPRs can be integrated with other non-destructive techniques for bridge deck inspection and evaluation [16]. Recently, a GPR is carried by a rover combining with additional sensors for planetary exploration [17]. However, the interpretation of a GPR image depends on the geometric relationship between the GPR and its world coordinate system. While most studies use the GPR as the only sensing modality and do not need to address extrinsic calibration problem, it is prudent that GPR extrinsic calibration problem should be addressed if the in-depth fusion of GPR data and other sensors are needed.

III. SYSTEM DESIGN AND PROBLEM FORMULATION

A. Calibration System Design and Procedure

The GPR extrinsic calibration has to be conducted while guaranteeing its output is in an Euclidean coordinate system, which means the surface has to be planar. To satisfy the calibration requirement, we have designed an artificial planar bridge as the calibration device (See Figure 2). The artificial bridge is made of wood and PVC because they do not impede radar signals and are strong enough to support the GPR survey cart to move on the bridge surface. Metal balls with a 1-inch (25.4 mm) diameter are chosen as calibration objects because they are insensitive to orientations and have good reflections to radar signals. The bridge allows us to freely adjust metal ball positions underneath the bridge to generate different inputs in the world coordinate system.

While the GPR moves on the platform to perform scanning, it senses metal balls under the wooden board and generates a GPR image. Each metal ball registers a hyperbola response in the GPR image, which serve as the input GPR measurements to the calibration problem. The calibration procedure contains three steps:

1) estimate hyperbola vertexes for each metal ball,
2) calculate metal ball coordinates with respect to the GPR coordinate system, and
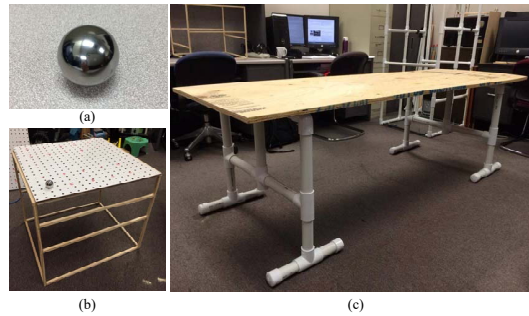3) estimate the rotation and the translation between the world and the GPR coordinates.

Fig. 2. (a) Calibration object (metal ball). (b) Calibration objects supported by a wooden framework. (c) Calibration platform.

B. Problem Definition

Let us define common notations before introducing the calibration problem. All 3D coordinate systems are right-handed coordinates as shown in Figure 3.
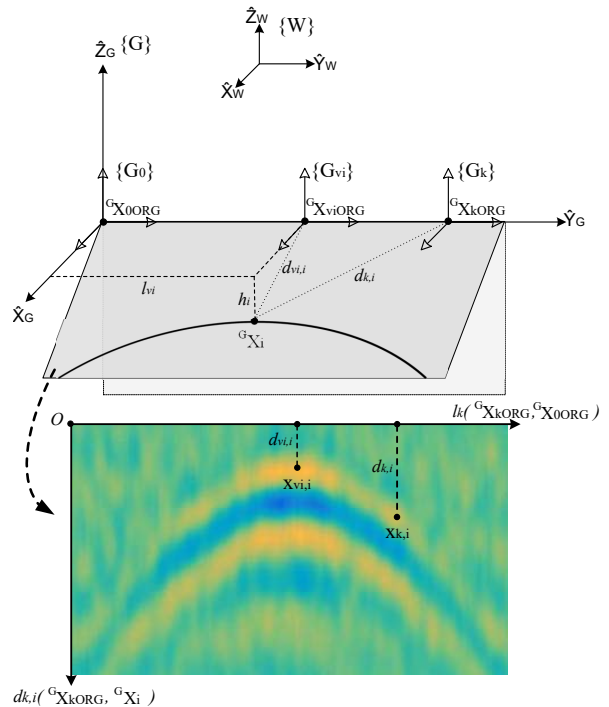

Fig. 3. Coordinate system relationships. Top: $\{W\}$, Middle: $\{G\}$ and GPR coordinate systems at each frame, Bottom: a sample GPR image.

1) $\{W\}$ denotes the Cartesian world coordinate system. $^{W}\mathbf{X}_i \in \mathbb{R}^3$ represents the i-th calibration point (located at the center of the metal ball i) with respect to $\{W\}$. As a convention, we will use the left superscript indicates the reference coordinate system in this paper.
2) $\{G\}$ denotes a coordinate system for interpreting GPR images and describes the GPR pose before it starts scanning, where the direction of its Y-axis is the GPR moving direction and its Z-axis is perpendicular to the bridge surface plane.
3) $\mathbf{x}_{k,i} \in \mathbb{R}^2$ denotes one point in the GPR image at frame k that corresponds to the i-th metal ball.

4) $\mathbf{H}_i = \{\mathbf{x}_{k,i} | 0 \le k \le m\}$ denotes a hyperbola, which is a set of points in GPR image.
5) $h_i \in \mathbb{R}^+$ denotes the vertical distance from $^W\mathbf{X}_i$ to the ground surface where the GPR is located.

We assume that:

a.1 In each scan, the GPR moves along Y-axis of $\{G\}$ on a planar surface during the calibration process. The distance traveled is provided by a wheel encoder. This guarantees $\{G\}$ is Cartesian and there exists a rigid body transform between $\{G\}$ and $\{W\}$.

a.2 Each GPR scan repeats exactly the same trajectory. This is guaranteed by forcing the survey cart to move along a fixed rail track with mechanical stops. This guarantees $\{G\}$ is the same across different scanning trials. Hence the data can be used together to estimate the $\{G\}$ to $\{W\}$ mapping.

a.3 The dielectric material is an uniform dielectric and the velocity of microwave is constant.

a.4 The measurement noise for metal balls and GPR readings are Gaussian distribution with zero means.

Now we can define our calibration problem:

Definition 1: Given n metal ball coordinates $^W\mathbf{X}_i$ with their vertical distance h_i, and their correspondence hyperbolas $\mathbf{H}_i$ in GPR images, $i = 1, 2, ..., n$, determine rigid body transformation from $\{W\}$ to $\{G\}$.

IV. CALIBRATION MODELING

We begin with modeling how a metal ball registers a hyperbola in the GPR image. Then we show how the metal ball positions can be recovered from the corresponding hyperbola. With enough corresponding metal ball positions in both $\{G\}$ and $\{W\}$, we can estimate the rigid body transformation between $\{G\}$ and $\{W\}$. We also analyze the error propagation in the process.

A. Modeling GPR Imaging Process

A GPR antenna contains a transmitter (TX) and a receiver (RX) as shown in Figure 4 [18]. We define $\{G_k\}$ as the GPR coordinate system at frame k, where its origin is the center of TX, its Y-axis is pointing from the origin to the center of RX, and its Z-axis is perpendicular to the plane where TX and RX are horizontally located. Let $^{G_k}\mathbf{X}_{kORG} \in \mathbb{R}^3$ denote the origin. We choose the GPR moving direction to the same as the Y-axis of $\{G_k\}$. As shown in Figure 3, all $\{G_k\}, k = 0, 1, 2, ...$ are iso-oriented and share the same Y-axis. $\{G\}$ overlaps with $\{G_0\}$ by design.
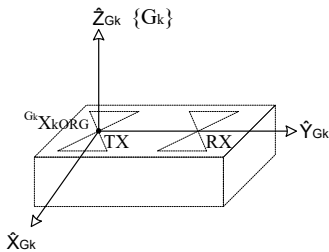

Fig. 4. GPR coordinate system at frame k.

When a GPR senses the echoed pulse from the i-th metal ball, it records two kinds of measurements. The first is GPR's traveled length l_k measured by its wheel encoder, where l_k is a function of GPR positions at frames 0 and k. The second is the microwave traveling time from TX to object to RX. Based on assumption **a.3**, the traveling time can be converted into the traveling distance. Besides, the TX-RX offset is usually a known intrinsic and pre-compensated in GPR images. Therefore, the microwave traveling time allows the GPR to output a half traveling distance $d_{k,i}$, where $d_{k,i}$ is the function of the GPR and the metal ball position. We can assemble l_k and $d_{k,i}$ into a vector $\mathbf{x}_{k,i}$ by

$$\mathbf{x}_{k,i} = \begin{bmatrix} l_k(^G\mathbf{X}_{0ORG}, {}^G\mathbf{X}_{kORG}) \\ d_{k,i}(^G\mathbf{X}_i, {}^G\mathbf{X}_{kORG}) \end{bmatrix} = \begin{bmatrix} \|^G\mathbf{X}_{0ORG} - {}^G\mathbf{X}_{kORG}\| \\ \|^G\mathbf{X}_i - {}^G\mathbf{X}_{kORG}\| \end{bmatrix}. \tag{1}$$

As shown at the bottom of Figure 3, a GPR image uses l_k as its horizontal axis and $d_{k,i}$ as its vertical axis. As the GPR moves, a hyperbola is generated. Moreover, let $\mathbf{x}_{v_i,i} = [l_{v_i}, d_{v_i,i}]^\mathsf{T}$ be the vertex of the hyperbola $\mathbf{H}_i$ that corresponds to $^G\mathbf{X}_i$, where v_i is the frame that generates $\mathbf{x}_{v_i,i}$, and $\{G_{v_i}\}$ is the GPR coordinate system at frame v_i as shown in Figure 3. We know that when the GPR is located at l_{v_i} along Y-axis, $d_{v_i,i}$ is the shortest distance from GPR to the i−th metal ball. Therefore, if the GPR moves from frame v_i to frame k, then we have $d_{k,i}^2 = d_{v_i,i}^2 + (l_k - l_{v_i})^2$, which can be described in a hyperbola form as

$$\tilde{\mathbf{x}}_{k,i}^\mathsf{T} \mathbf{Q}_i \tilde{\mathbf{x}}_{k,i} = 0, \tag{2}$$

where $\tilde{\mathbf{x}}_{k,i} = [l_k, d_{k,i}, 1]^\mathsf{T}$, and $\mathbf{Q}_i = \begin{bmatrix} 1 & 0 & -l_{v_i} \\ 0 & -1 & 0 \\ -l_{v_i} & 0 & l_{v_i}^2 + d_{v_i,i}^2 \end{bmatrix}$. For a general conic equation $ax^2 + bxy + cy^2 + dx + ey + f = 0$ with 5 DoFs, the DoFs in our case decreases to two because $b = 0$, $e = 0$, and $a = -c = 1$. So two parameters $\{l_{v_i}, d_{v_i,i}\}$ are sufficient to define the corresponding hyperbola.

B. Estimating Hyperbolas from GPR Images

Before estimating $\mathbf{x}_{vi,i} = [l_{v_i}, d_{v_i,i}]^\mathsf{T}$ from hyperbola $\mathbf{H}_i = \{\mathbf{x}_{k,i} | 0 \le k \le m\}$, we compensate the metal ball radius r when computing $d_{k,i}$ (the reading from GPR image) by denoting $\tilde{d}_{k,i} = d_{k,i} + r$ as the real distance from $^G\mathbf{X}_i$ to $^G\mathbf{X}_{kORG}$. When the GPR moves to perform the scanning, k changes and generates a sequence of $\tilde{\mathbf{x}}_{k,i}$ as inputs. We model $\mathbf{x}_{k,i}$'s measurement error as a zero mean Gaussian with covariance matrix $\sigma_{k,i}^2 \mathbf{I}$. Because r is a constant, the noise distribution of $\tilde{d}_{k,i}$ is the same as that of $d_{k,i}$. Stacking all measurements together to estimate $\mathbf{x}_{vi,i}$, the overall measurement error function is,

$$C(\mathbf{x}_{vi,i}) = \begin{bmatrix} \tilde{\mathbf{x}}_{0,i}^\mathsf{T} \mathbf{Q}_i \tilde{\mathbf{x}}_{0,i} \\ \vdots \\ \tilde{\mathbf{x}}_{m,i}^\mathsf{T} \mathbf{Q}_i \tilde{\mathbf{x}}_{m,i} \end{bmatrix}. \tag{3}$$

The maximum-likelihood estimation (MLE) of $\mathbf{x}_{vi,i}$ is obtained by minimizing the following Mahalanobis Distance

$$\mathbf{x}_{vi,i}^* = \underset{\mathbf{x}_{vi,i}}{\operatorname{argmin}} \ C(\mathbf{x}_{vi,i})^\mathsf{T} \Sigma_i^{-1} C(\mathbf{x}_{vi,i}), \tag{4}$$

where $\Sigma_i = diag(\sigma_{0,i}^2, \sigma_{1,i}^2, \ldots, \sigma_{m,i}^2)$ is a diagonal matrix. This problem can be solved by applying the Levenberg-Marquardt (LM) algorithm or any nonlinear optimization solver.

We also analyze the error of the estimated hyperbola vertex using the error backward propagation [19] under Gaussian assumptions. The covariance matrix of $\mathbf{x}_{vi,i}^*$ can be obtained as follows,

$$\Sigma_{vi} = \left(J_C^T \Sigma_i^{-1} J_C\right)^{-1}, \tag{5}$$

where Jacobian matrix

$$J_C = \left.\frac{\partial C}{\partial \mathbf{x}_{vi,i}}\right|_{\mathbf{x}_{vi,i}=\mathbf{x}_{vi,i}^*} = \begin{bmatrix} 2(l_{v_i}-l_0) & 2d_{v_i} \\ \vdots & \vdots \\ 2(l_{v_i}-l_m) & 2d_{v_i} \end{bmatrix}.$$

C. Recovering Metal Ball Positions in $\{G\}$

As shown in Figure 3, the vertical component of the hyperbola vertex in the GPR image represents the shortest distance from the GPR Y-axis to the metal ball in $\{G\}$ during the scanning. Given the vertical height h_i, the metal ball position in $\{G\}$ is given by

$$^G\mathbf{X}_i = \begin{bmatrix} x_i \\ y_i \\ z_i \end{bmatrix} = \begin{bmatrix} \sqrt{d_{v_i,i}^2 - h_i^2} \\ l_{v_i} \\ h_i \end{bmatrix}. \tag{6}$$

Since $^G\mathbf{X}_i$ is a function of $[\mathbf{x}_{vi,i}^T, h_i]^T$, its uncertainty depends on the noise distribution of $[\mathbf{x}_{vi,i}^T, h_i]^T$. The covariance matrix of $\mathbf{x}_{vi,i}$ is Σ_{vi} by (5). Let the noise distribution of h_i be a zero mean Gaussian with variance σ_i^2. Because the measurement noise of $\mathbf{x}_{vi,i}$ and h_i are independent, we have

$$cov\left(\begin{bmatrix} l_{v_i} \\ d_{v_i,i} \\ h_i \end{bmatrix}\right) = \begin{bmatrix} \Sigma_{vi} & \mathbf{0} \\ \mathbf{0} & \sigma_i^2 \end{bmatrix} \tag{7}$$

where $cov(\cdot)$ indicates the covariance matrix of a random vector. Applying the first-order approximation of error forward propagation [19], we obtain the covariance matrix $^G\Sigma_i$ of $^G\mathbf{X}_i$,

$$^G\Sigma_i = J_H cov\left(\begin{bmatrix} l_{v_i} \\ d_{v_i,i} \\ h_i \end{bmatrix}\right) J_H^T, \tag{8}$$

where Jacobian matrix

$$J_H = \frac{\partial\, ^G\mathbf{X}_i}{\partial (l_{v_i}, d_{v_i,i}, h_i)} = \begin{bmatrix} 0 & \frac{d_{v_i,i}}{\sqrt{d_{v_i,i}^2-h_i^2}} & \frac{-h_i}{\sqrt{d_{v_i,i}^2-h_i^2}} \\ 1 & 0 & 0 \\ 0 & 0 & 1 \end{bmatrix}.$$

$^G\Sigma_i$ characterizes the uncertainty of $^G\mathbf{X}_i$.

D. Estimating Rigid Body Transformation from $\{W\}$ to $\{G\}$

Given n correspondence points $\{^W\mathbf{X}_i \leftrightarrow {}^G\mathbf{X}_i | i = 1, 2 \ldots n\}$, where $^W\mathbf{X}_i$ is obtained through direct measurements, we are able to estimate the rigid body transformation $^G_W\mathbf{T}$ from $\{W\}$ to $\{G\}$. Through $^G_W\mathbf{T}$, $^G\mathbf{X}_i$ can be represented by

$$^G\mathbf{X}_i = {}^G_W\mathbf{T}(^W\mathbf{X}_i) = {}^G_W\mathbf{R}\,^W\mathbf{X}_i + {}^G_W\mathbf{t}, \tag{9}$$

where $^G_W\mathbf{R}$ is the rotation matrix and $^G_W\mathbf{t}$ the translation vector. First, the closed-form solutions of $^G_W\mathbf{R}$ and $^G_W\mathbf{t}$ are computed by Horn's method [20]. Let the covariance matrix of $^W\mathbf{X}_i$ be $^W\Sigma_i$. The parameter vector to be estimated is defined as $\mathbf{p} = [\xi^T, {}^W\hat{\mathbf{X}}_1^T, {}^W\hat{\mathbf{X}}_2^T, \cdots, {}^W\hat{\mathbf{X}}_n^T]^T$, where $\xi = [\theta_x, \theta_y, \theta_z, t_x, t_y, t_z]^T$ is the six-vector representation of $^G_W\hat{\mathbf{R}}$ and $^G_W\hat{\mathbf{t}}$, $(\theta_x, \theta_y, \theta_z)$ is the Euler angle representation of $^G_W\hat{\mathbf{R}}$ in the order of Z-Y-X, and $[t_x, t_y, t_z]^T = {}^G_W\hat{\mathbf{t}}$. Then, we estimate $^W\hat{\mathbf{X}}_i$, $^G_W\hat{\mathbf{R}}$, and $^G_W\hat{\mathbf{t}}$ by minimizing the cost function

$$\omega(\mathbf{p}) = \begin{bmatrix} ^W\hat{\mathbf{X}}_1 - {}^W\mathbf{X}_1 \\ \vdots \\ ^W\hat{\mathbf{X}}_n - {}^W\mathbf{X}_n \\ ^G_W\mathbf{T}(^W\hat{\mathbf{X}}_1) - {}^G\mathbf{X}_1 \\ \vdots \\ ^G_W\mathbf{T}(^W\hat{\mathbf{X}}_n) - {}^G\mathbf{X}_n \end{bmatrix}. \tag{10}$$

The MLE of $\mathbf{p}$ is solved by minimizing the following problem

$$\mathbf{p}^* = \underset{\mathbf{p}}{\arg\min}\ \omega(\mathbf{p})^T \Sigma_\omega^{-1} \omega(\mathbf{p}), \tag{11}$$

where $\Sigma_\omega = diag(^W\Sigma_1, \cdots, {}^W\Sigma_n, {}^G\Sigma_1, \cdots, {}^G\Sigma_n)$ is a block-wise diagonal matrix. $^W\Sigma_i$ is the covariance matrix of the ground truth measurement, which is a function of ruler resolution and material deformation. $^G\Sigma_i$ can be obtained from (8). This problem is then solved by LM algorithm. Lemma 1 shows how to estimate $cov(\xi)$, the covariance matrix of ξ.

Lemma 1: Under the Gaussian noise assumption, the covariance matrix of ξ is

$$cov(\xi) = (\mathbf{A} - \mathbf{B}\mathbf{D}^{-1}\mathbf{C})^{-1} \tag{12}$$

where

$$\mathbf{A} = \sum_{i=1}^n \left(\frac{\partial\, ^G_W\mathbf{T}(^W\hat{\mathbf{X}}_i)}{\partial \xi}\right)^T \left(^G\Sigma_i^{-1}\right) \left(\frac{\partial\, ^G_W\mathbf{T}(^W\hat{\mathbf{X}}_i)}{\partial \xi}\right),$$

$$\mathbf{B} = \begin{bmatrix} \left(\frac{\partial\, ^G_W\mathbf{T}(^W\hat{\mathbf{X}}_1)}{\partial\, ^W\hat{\mathbf{X}}_1}\right)^T \left(^G\Sigma_1^{-1}\right) \left(\frac{\partial\, ^G_W\mathbf{T}(^W\hat{\mathbf{X}}_1)}{\partial \xi}\right) \\ \vdots \\ \left(\frac{\partial\, ^G_W\mathbf{T}(^W\hat{\mathbf{X}}_n)}{\partial\, ^W\hat{\mathbf{X}}_n}\right)^T \left(^G\Sigma_n^{-1}\right) \left(\frac{\partial\, ^G_W\mathbf{T}(^W\hat{\mathbf{X}}_n)}{\partial \xi}\right) \end{bmatrix}^T,$$

$$\mathbf{C} = \begin{bmatrix} \left(\frac{\partial\, ^G_W\mathbf{T}(^W\hat{\mathbf{X}}_1)}{\partial\, ^W\hat{\mathbf{X}}_1}\right)^T \left(^G\Sigma_1^{-1}\right) \left(\frac{\partial\, ^G_W\mathbf{T}(^W\hat{\mathbf{X}}_1)}{\partial \xi}\right) \\ \vdots \\ \left(\frac{\partial\, ^G_W\mathbf{T}(^W\hat{\mathbf{X}}_n)}{\partial\, ^W\hat{\mathbf{X}}_n}\right)^T \left(^G\Sigma_n^{-1}\right) \left(\frac{\partial\, ^G_W\mathbf{T}(^W\hat{\mathbf{X}}_n)}{\partial \xi}\right) \end{bmatrix},$$

$$\mathbf{D} = diag\left(^W\Sigma_1^{-1} + \left(\frac{\partial\, ^G_W\mathbf{T}(^W\hat{\mathbf{X}}_1)}{\partial\, ^W\hat{\mathbf{X}}_1}\right)^T \left(^G\Sigma_1^{-1}\right) \left(\frac{\partial\, ^G_W\mathbf{T}(^W\hat{\mathbf{X}}_1)}{\partial\, ^W\hat{\mathbf{X}}_1}\right),\right.$$
$$\left.\cdots, {}^W\Sigma_n^{-1} + \left(\frac{\partial\, ^G_W\mathbf{T}(^W\hat{\mathbf{X}}_n)}{\partial\, ^W\hat{\mathbf{X}}_n}\right)^T \left(^G\Sigma_n^{-1}\right) \left(\frac{\partial\, ^G_W\mathbf{T}(^W\hat{\mathbf{X}}_n)}{\partial\, ^W\hat{\mathbf{X}}_n}\right)\right).$$

Proof: From the first order approximation of error backward propagation [19], we can obtain the covariance

matrix of $\mathbf{p}^*$ by

$$cov(\mathbf{p}^*) = (J_\omega^T \Sigma_\omega^{-1} J_\omega)^{-1} \qquad (13)$$

where

$$J_\omega = \frac{\partial \omega}{\partial \mathbf{p}}$$

$$= \begin{bmatrix} \mathbf{0} & \mathbf{I}_3 & \mathbf{0} & \mathbf{0} \\ \vdots & \mathbf{0} & \ddots & \mathbf{0} \\ \mathbf{0} & \mathbf{0} & \mathbf{0} & \mathbf{I}_3 \\ \hline \frac{\partial {}_W^G\mathbf{T}({}^W\hat{\mathbf{X}}_1)}{\partial \xi} & \frac{\partial {}_W^G\mathbf{T}({}^W\hat{\mathbf{X}}_1)}{\partial {}^W\hat{\mathbf{X}}_1} & \mathbf{0} & \mathbf{0} \\ \vdots & \mathbf{0} & \ddots & \mathbf{0} \\ \frac{\partial {}_W^G\mathbf{T}({}^W\hat{\mathbf{X}}_n)}{\partial \xi} & \mathbf{0} & \mathbf{0} & \frac{\partial {}_W^G\mathbf{T}({}^W\hat{\mathbf{X}}_n)}{\partial {}^W\hat{\mathbf{X}}_n} \end{bmatrix}_{6n \times (3n+6)}$$

where $\mathbf{I}_3$ is a 3×3 identity matrix, and $\mathbf{0}$ is the zero matrix.

In order to solve the covariance matrix of ξ, we need to derive it from $cov(\mathbf{p}^*)$. According to J_ω in (13) and $\Sigma_\omega^{-1} = diag({}^W\Sigma_1^{-1}, \cdots, {}^W\Sigma_n^{-1}, {}^G\Sigma_1^{-1}, \cdots, {}^G\Sigma_n^{-1})$, we have

$$J_\omega^T \Sigma_\omega^{-1} J_\omega = \begin{bmatrix} \mathbf{A} & \mathbf{B} \\ \hline \mathbf{C} & \mathbf{D} \end{bmatrix} \qquad (14)$$

Through the block-wise matrix inversion, we can derive the covariance matrix of ξ using (12). ∎

E. Rigid Body Transformation Model Error

Let ${}^G\hat{\mathbf{X}}_i$ be the model prediction of ${}^G\mathbf{X}_i$, which is obtained by (12) using calibrated parameters and ground truth measurements ${}^W\mathbf{X}_i$ in $\{W\}$. To verify extrinsic calibration results, we define the Euclidean distance between ${}^G\hat{\mathbf{X}}_i$ and ${}^G\mathbf{X}_i$ as the metric function for the model prediction error ε_i

$$\varepsilon_i = f({}^G\hat{\mathbf{X}}_i, {}^G\mathbf{X}_i) = \| {}^G\hat{\mathbf{X}}_i - {}^G\mathbf{X}_i \|. \qquad (15)$$

Lemma 2 shows the variance of ε_i.

Lemma 2: Under Gaussian noise assumption, the variance of ε_i is denoted by

$$\sigma_{\varepsilon_i}^2 = J_{\hat{G}} {}^G\hat{\Sigma}_i J_{\hat{G}}^T + J_G {}^G\Sigma_i J_G^T, \qquad (16)$$

where $J_{\hat{G}} = \frac{\partial f}{\partial {}^G\hat{\mathbf{X}}_i}$ and $J_G = \frac{\partial f}{\partial {}^G\mathbf{X}_i}$.

Proof: Since ε_i is a function of ${}^G\hat{\mathbf{X}}_i$ and ${}^G\mathbf{X}_i$, the uncertainty of ε_i comes from their corresponding covariance matrices ${}^G\hat{\Sigma}_i$ and ${}^G\Sigma_i$. ${}^G\Sigma_i$ is derived from GPR image with vertical distance h_i as shown in (8). ${}^G\hat{\Sigma}_i$ is caused by parameter uncertainty of ξ and measurement errors from ${}^W\mathbf{X}_i$. Because ξ is obtained from the calibrating set and ${}^W\mathbf{X}_i$ is obtained separately for testing the calibration model, there is no dependence between ξ and ${}^W\mathbf{X}_i$. Therefore, by the forward propagation of error [19] under first-order approximation, ${}^G\hat{\Sigma}_i$ is obtained as follows

$$ {}^G\hat{\Sigma}_i = J_\xi cov(\xi) J_\xi^T + J_W {}^W\Sigma_i J_W^T \qquad (17)$$

where $J_\xi = \frac{\partial {}_W^G\mathbf{T}({}^W\mathbf{X}_i)}{\partial \xi}$, $J_W = \frac{\partial {}_W^G\mathbf{T}({}^W\mathbf{X}_i)}{\partial {}^W\mathbf{X}_i}$, $cov(\xi)$ is the covariance matrix of ξ from Lemma 1, and ${}^W\Sigma_i$ is the covariance

matrix of ${}^W\mathbf{X}_i$. Because ${}^G\hat{\mathbf{X}}_i$ and ${}^G\mathbf{X}_i$ are independent, the variance of ε_i can be obtained from (19) using the first order approximation of error forward propagation [19]. ∎

V. EXPERIMENTS

A. Experiment Setup

The GPR system is a GSSI SIR-3000 with 1.6 GHz antennas and is mounted on a GSSI model 623 survey cart with a wheel encoder. The parameters are set in GPR control unit as follows: the horizontal sample rate is 390 frames/meter, the two-way travel time is 8 ns, the sample rate is 1024 sample/frame, and the dielectric constant is 1. The radius of metal balls, r, is 12.7 mm. ${}^W\mathbf{X}_i$ and h_i are measured manually in our laboratory. We repeat the experiment for 80 times, and each time we place one metal ball on the pegboard in different positions ${}^W\mathbf{X}_i$. Each time the GPR follows the same trajectory with the metal ball located at different positions.

We use RADAN 7 from GSSI to export GPR images. In the pre-processing stage, we collect the GPR image without metal balls as the background. It allows us to apply the background subtraction to obtain clearer hyperbolas. Besides, $\mathbf{H}_i$ in each hyperbola are obtained first by manually selecting a region containing the hyperbola, and then by automatic detection through searching the peak reception for each selected frame. Overall, we collect 80 sets and each set consists of $\mathbf{H}_i$, ${}^W\mathbf{X}_i$ and h_i.

To validate the calibration results, we divide the 80 sets into two groups: half of them as the training set and the rest as the testing set. The training set is to estimate extrinsic parameters of the GPR and the testing set is to verify the calibration results.

B. Calibration Results, Model Prediction Errors, and Uncertainty Analysis Results

We estimate ${}_W^G\mathbf{R}$ and ${}_W^G\mathbf{t}$ by using the training set. Recall that $(\theta_x, \theta_y, \theta_z)$ is the Euler angle representation of ${}_W^G\mathbf{R}$, the calibration result shows that ${}_W^G\mathbf{t} = [170.9, 199.5, -342.0]^T$, $[\theta_x, \theta_y, \theta_z]^T = [-0.0153, -0.0032, 1.5589]^T$, and the units are in mm and rad respectively.

In order to verify the extrinsic parameters, we take the GPR images in the testing set to compute the i-th metal ball coordinates ${}^G\mathbf{X}_i$, and regard it as the ground truth. On the other hand, we use ${}_W^G\mathbf{R}$ and ${}_W^G\mathbf{t}$ from the training set to compute ${}^G\hat{\mathbf{X}}_i$ based on ${}^W\mathbf{X}_i$ in the testing set using (12). As shown in Figure 5, the red points represent ${}^G\hat{\mathbf{X}}_i$ and the blue points represent ${}^G\mathbf{X}_i$. The mean and the standard deviation (SD) of errors for the testing set are 9.77 mm and 2.94 mm, respectively. Testing results are also shown in Figure 5 and Table I. Considering the fact that the GPR signal wave length is 18.8 cm, the result is satisfying.

We also evaluate if our uncertainty analysis in Section IV-E can capture the prediction error of the calibrated model. We have the error and the predicted SD from Lemma 2 for the 40 testing samples listed in Table I. More specifically, the measurement errors for metal ball position measurements
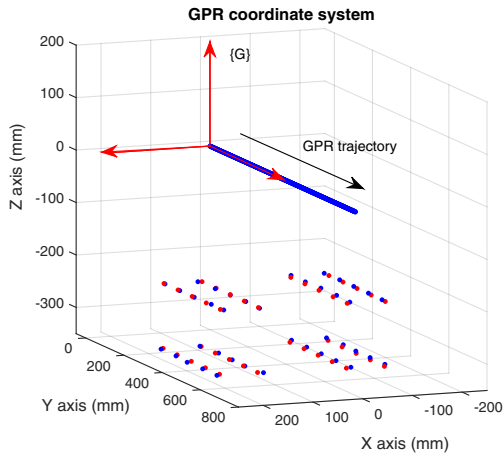
Fig. 5. The red points represent $^{G}\hat{\mathbf{X}}_i$, and the blue points represent $^{G}\mathbf{X}_i$.

have a variance of 12 mm^2 in each dimension. This is caused by limited resolution of our ruler and structural deformation under weight. Thus for all i, $^{W}\Sigma_i = 12\mathbf{I_3}$, and $\sigma_i^2 = 12$ for h_i. Besides, the variance for the points on GPR image is set to $\sigma_{k,i}^2 = 1$. The results agree with our analysis as 70% errors fall in the 1-σ range of the calibrated model prediction.

TABLE I

THE PREDICTED SD OF ε_i VS ITS ACTUAL VALUE

i	σ_{ε_i}(mm)	ε_i(mm)	i	σ_{ε_i}(mm)	ε_i(mm)
1	9.08	6.41	21	9.56	7.81
2	8.24	3.89	22	8.46	8.34
3	12.26	9.46	23	10.33	8.53
4	7.82	7.90	24	7.60	9.96
5	8.50	8.63	25	6.87	13.77
6	29.49	9.75	26	35.68	9.22
7	26.53	9.34	27	18.36	2.41
8	23.49	7.34	28	11.79	4.17
9	47.46	9.64	29	13.16	6.53
10	42.16	14.44	30	16.56	5.53
11	24.09	12.95	31	47.49	11.89
12	28.22	10.34	32	21.05	13.22
13	22.27	10.27	33	14.01	17.32
14	26.65	8.96	34	14.75	12.38
15	25.25	10.39	35	12.06	9.84
16	20.66	11.58	36	7.10	12.34
17	19.02	9.13	37	6.78	10.82
18	13.82	11.66	38	6.04	11.15
19	12.39	12.59	39	7.32	9.40
20	10.19	11.46	40	7.21	9.79

VI. CONCLUSIONS AND FUTURE WORK

We proposed system design, procedure and models for the extrinsic calibration of a GPR. We designed an artificial planar bridge as the calibration device. Using metal balls as calibration objects, we modeled the GPR imaging process and extracted hyperbolas in the GPR image to recover metal ball coordinates in the GPR coordinate system. The MLE is employed to estimate the rigid body transformation. We provided the closed form error analysis for our calibration models. The physical experiments confirmed our results.

In the future, we will develop algorithms to calibrate a GPR and a camera simultaneously. We will fuse the data from different senors for automatic in-traffic bridge inspection.

REFERENCES

[1] A. Elatta, L. P. Gen, F. L. Zhi, Y. Daoyuan, and L. Fei, "An overview of robot calibration," *Information Technology Journal*, vol. 3, no. 1, pp. 74–78, January 2004.
[2] S. Ross, *Introduction to Probability Models, Ninth Edition*. Academic Press, 2007.
[3] B. Siciliano and O. Khatib, *Springer handbook of robotics*. Springer Science & Business Media, 2008.
[4] D. Song, N. Qin, and K. Goldberg, "A minimum variance calibration algorithm for pan-tilt robotic cameras in natural environments," in *IEEE International Conference on Robotics and Automation (ICRA), Orlando, Florida*, May 2006.
[5] K. H. Strobl and G. Hirzinger, "Optimal hand-eye calibration," in *IEEE/RSJ International Conference on Intelligent Robots (IROS), Beijing, China*, 2006, pp. 4647–4653.
[6] J. Fraden, *Handbook of modern sensors: physics, designs, and applications*. Springer Science & Business Media, 2004.
[7] Z. Zhang, "A flexible new technique for camera calibration," *IEEE Transactions on Pattern Analysis and Machine Intelligence*, vol. 22, no. 11, pp. 1330–1334, 2000.
[8] D. Song, C. Kim, and J. Yi, "Simultaneous localization of multiple unknown and transient radio sources using a mobile robot," *IEEE Transactions on Robotics*, vol. 28, no. 3, pp. 668–680, June 2012.
[9] C. Gao and J. R. Spletzer, "On-line calibration of multiple lidars on a mobile vehicle platform," in *IEEE International Conference on obotics and Automation (ICRA), Anchorage, AK*, 2010, pp. 279–284.
[10] Q. Zhang and R. Pless, "Extrinsic calibration of a camera and laser range finder (improves camera calibration)," in *IEEE/RSJ International Conference on Intelligent Robots (IROS), Sendai, Japan*, vol. 3, 2004, pp. 2301–2306.
[11] D. J. Daniels, *Ground penetrating radar, 2nd Edition*. The Institution of Engineering and Technology, 2004, vol. 1.
[12] H. M. Jol, *Ground penetrating radar theory and applications*. Elsevier, 2008.
[13] A. Annan, *Electromagnetic principles of ground penetrating radar*. Elsevier, 2009, vol. 1.
[14] T. Fukuda, Y. Hasegawa, K. Kosuge, K. Komoriya, F. Kitagawa, and T. Ikegami, "Environment-adaptive antipersonnel mine detection system-advanced mine sweeper," in *IEEE/RSJ International Conference on Intelligent Robots (IROS), Beijing, China*, 2006, pp. 3618–3623.
[15] T. Evans, R. Ponticelli, E. Garcia, P. Gonzalez de Santos, and M. Armada, "A scanning robotic system for humanitarian de-mining activities," *Industrial Robot: An International Journal*, vol. 35, no. 2, pp. 133–142, 2008.
[16] H. M. La, N. Gucunski, S.-H. Kee, J. Yi, T. Senlet, and L. Nguyen, "Autonomous robotic system for bridge deck data collection and analysis," in *IEEE/RSJ International Conference on Intelligent Robots (IROS), Chicago, IL*, 2014, pp. 1950–1955.
[17] P. Furgale, T. D. Barfoot, N. Ghafoor, K. Williams, and G. Osinski, "Field testing of an integrated surface/subsurface modeling technique for planetary exploration," *The International Journal of Robotics Research*, vol. 29, no. 12, pp. 1529–1549, October 2010.
[18] C. Warren and A. Giannopoulos, "Investigation of the directivity of a commercial ground-penetrating radar antenna using a finite-difference time-domain antenna model," in *14th International Conference on Ground Penetrating Radar (GPR)*, 2012, pp. 226–231.
[19] R. Hartley and A. Zisserman, *Multiple View Geometry in Computer Vision, 2nd Edition*. Cambridge University Press, 2004.
[20] B. Horn, "Closed form solution of absolute orientation using unit quaternions," *Journal of the Optical Society A*, vol. 4, no. 4, pp. 629–42, 1987.